

PMGS: Reconstruction of Projectile Motion across Large Spatiotemporal Spans via 3D Gaussian Splatting

Yijun Xu^{†1}, Jingrui Zhang^{†2}, Yuhan Chen³, Dingwen Wang^{*2}, Lei Yu^{*4} and Chu He^{*1}

¹School of Electronic Information, Wuhan University

²School of Computer Science, Wuhan University

³College of Mechanical and Vehicle Engineering, Chongqing University

⁴School of Artificial Intelligence, Wuhan University

Abstract

Modeling complex rigid motion across large spatiotemporal spans remains an unresolved challenge in dynamic reconstruction. Existing paradigms are mainly confined to short-term, small-scale deformation and offer limited consideration for physical consistency. This study proposes **PMGS**, focusing on reconstructing **P**rojectile **M**otion via **3D G**aussian **S**platting. The workflow comprises two stages: 1) Target Modeling: achieving object-centralized reconstruction through dynamic scene decomposition and an improved point density control; 2) Motion Recovery: restoring full motion sequences by learning per-frame SE(3) poses. We introduce an acceleration consistency constraint to bridge Newtonian mechanics and pose estimation, and design a dynamic simulated annealing strategy that adaptively schedules learning rates based on motion states. Furthermore, we devise a Kalman fusion scheme to optimize error accumulation from multi-source observations to mitigate disturbances. Experiments show PMGS's superior performance in reconstructing high-speed nonlinear rigid motion compared to mainstream dynamic methods.

1 Introduction

Dynamic reconstruction has become an engine driving modern film animation, game interaction, and virtual reality. The rise of neural rendering has pushed reconstruction fidelity to unprecedented heights, enabling the depiction of highly

[†] These authors contributed equally to this work.

^{*} Corresponding authors: Chu He (chuhe@whu.edu.cn), Dingwen Wang (wangdw@whu.edu.cn) and Lei Yu (ly.wd@whu.edu.cn)

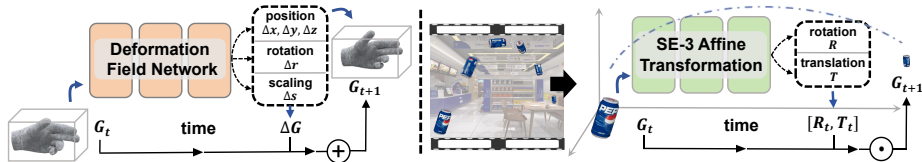


Figure 1: Left: Current paradigms focus on small-scale deformation reconstruction. Right: PMGS explores complex rigid motion modeling across large spatiotemporal spans.

challenging deformations, such as subtle tremors in biological tissues [9]. Meanwhile, breakthroughs in generative methods [24, 2] have achieved controllable synthesis of dynamic scenes with diverse artistic styles, vastly expanding the boundary of imagination in visual expression.

However, returning to a task related to the essential laws of the physical world: **reconstruction of complex rigid motions over large spatiotemporal spans**—remains an insufficiently explored challenging issue. The difficulties lie in: 1) Modeling paradigm; 2) Physical consistency.

Most existing modeling paradigms are designed for small range non-rigid motion over short time spans [21, 14, 32, 30]. These approaches rely on deformation fields with complex temporal regularization to achieve spatiotemporal alignment. However, discrete sampling struggles to capture large nonlinear motion (e.g., accelerated rotation), often resulting in noticeable artifacts and trajectory fragmentation when modeling high-speed rigid motion [30]. Additionally, current 4D datasets exhibit similar limitations: in most scenarios, moving objects occupy only a small portion of the scene and exhibit minimal movement. Consequently, many methods prioritize optimizing appearance similarity metrics rather than addressing the core challenge of accurate motion recovery.

The absence of physical consistency poses another major challenge. Many works focus on optimizing appearance similarity while neglecting the pervasive physical constraints in the real world. However, when modeling complex motion across large spatiotemporal spans, relying solely on photometric supervision fails to constrain the vast 3D solution space effectively. For NeRF-based methods [26, 14, 20], the inherent characteristics of implicit representations encode motion cues within black-box network weights, making physical interactions difficult to model and unintuitive. The introduction of 3D Gaussian Splatting (3DGS) [11] has partially addressed this by combining explicit point-based representations with neural rendering, thereby providing a structured carrier for scene understanding. Consequently, some GS-based approaches [9, 5, 17] incorporate off-the-shelf models to enhance physical realism. We argue that this model-stacking strategy introduces compounded uncertainties by layering new approximations over existing ones. More critically, it bypasses the exploration of fundamental physical principles, ultimately reducing the reconstruction task to uninterpretable compensatory computations.

To tackle these issues, we selected a representative task for focused solutions:

Projectile motion. As a fundamental concept in mechanics, it describes an object launched with an initial velocity, following parabolic motion under gravity. The study extends from free-fall to complex situations with self-rotation. This phenomenon is not only ubiquitous in real world (e.g., falling objects from heights, throwing events in sports, military ballistic trajectories), while also encompasses the typical challenges of rigid motion, including variable speed, large span, and compound motion (translation and rotation). Consequently, this archetypal paradigm can be generalized to any dynamic scenario within constant force fields in nature, demonstrating universal applicability.

In this paper, we focus on the modeling of complex rigid motions with large spatiotemporal spans, and propose **PMGS**, a framework that reconstructs **P**rojectile **M**otion via **3D G**aussian **S**platting. By leveraging temporal continuity in video sequences and explicit Gaussian representation, we estimate per-frame $SE(3)$ affine transformation throughout the motion which fundamentally unattainable with NeRF-based methods. Guided by first principles of physics, we introduce an acceleration constraint for motion recovery. Additionally, to alleviate issues of learning oscillations and trajectory fractures caused by fixed training paradigms, we develop a Dynamic Simulated Annealing (DSA) strategy that adaptively schedules the training process based on real-time velocity and displacement variations. Departing from conventional methods that treat physical constraints merely as regularization components, we propose a Kalman filter-based optimal estimation scheme to fuse cross-modal observations thereby minimizing potential disturbances.

Overall, our main contributions can be outlined as:

- We propose PMGS, a framework integrating target modeling and motion recovery to reconstruct projectile motion. Particularly, we contribute a dataset designed for complex rigid motion modeling at large spatiotemporal scales—an area notably underserved by existing datasets.
- We introduce an acceleration consistency constraint connecting Newtonian mechanics to pose estimation. Our DSA strategy dynamically adapts training via velocity-displacement motion states, addressing fixed paradigms’ nonlinear motion limitations.
- We design a Kalman fusion scheme is to dynamically optimize multi-source observations with adaptive weighting, minimizing error accumulation caused by real-world disturbances or training oscillations.

2 Related Work

2.1 3D Representation.

[19, 16] pioneered the exploration of the implicit radiance fields. The milestone work, NeRF [18], maps spatial coordinates and viewing directions to color and density through the MLP, enabling differentiable and compact units of complex

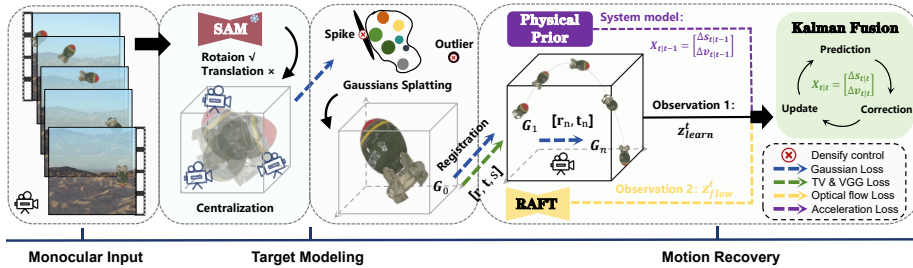


Figure 2: Overview of PMGS. We first segment the target then decompose the motion through centralization to transform the dynamic scene into static. For modeling, we learn a set of Gaussian kernels and align them at the original scale with a set of learnable affine transformation. In the motion recovery, we estimate the target’s SE(3) transformation frame by frame, and comprehensively improve tracking accuracy by integrating physics-enhanced strategies.

scenes. However, the implicit representations are inherently constrained in geometric nature, which limits their exploration for editing and interaction. Instead, 3DGS [11] introduces a shift from implicit to explicit paradigm, the point-based representation greatly expands its potential of scene understanding.

2.2 Dynamic Neural Rendering.

Current dynamic neural rendering include: (1) Point deformation fields [21] map sampled points at each timestep to a static canonical space. (2) Time-aware Volume Rendering [14, 26] employs factorized voxels to independently compute features for each point. (3) The Gaussian deformation field [32, 37, 7] transforms 3D Gaussians to their target position at specific timesteps. The critical issues lie in the deformation field struggles to model large inter-frame displacements that commonly occur in real-world scenarios, which can be further validated by experiments on Panoptic Studio dataset [10] conducted by 4DGS [30]. Moreover, due to the lack of physical consistency constraints, the network tends to focus on fitting appearance similarity while neglecting structural accuracy at the geometric level. As a typical example, when there are large areas of nearly uniform color, Gaussian bodies will float chaotically within regions of similar color [15].

2.3 Enhancing GS with Physical Assistance.

Introducing physical assistance to enhance 3DGS has been widely applied. [5, 9, 38] utilize off-the-shelf monocular depth estimation models [23] for scene initialization or sparse reconstruction. [36] devised a Spring-Mass model to simulate the elastic objects’s falling and collision. [17] is designed for 3D dataset generation which integrates the PyBullet engine to emulate the placement of objects and their dynamic processes. [2, 31] enhances pose estimation by ensuring

scale consistency and local rigidity. Essentially, current approaches use rough approximations from external physics models to fix ill-posed inverse problems in vision systems. Nevertheless, pre-trained engines lose confidence sharply in unusual scenarios, and their black-box makes errors untraceable—causing mistakes to snowball. Differently, we propose to explore strategies grounded directly in first principles of physics [22], rather than relying on external models for unreliable assistance.

3 Method

PMGS takes a monocular video as input to reconstruct the target and achieve full-sequence projectile motion recovery. For modeling appearance and geometry, we equivalently convert dynamic scenes into static through motion decomposition, and combined with the improved point density control strategy to enhance the geometric accuracy. During motion recovery, we leverage video temporal continuity and the explicit Gaussian representation to estimate per-frame $SE(3)$ transformations. To ensure physically consistent pose learning, we introduce an acceleration consistency constraint that establishes direct connections between pose estimation and Newtonian dynamics priors. Furthermore, we devise a DSA strategy, which adaptively schedules the optimization process according to real-time motion states. Finally, we design a Kalman fusion strategy to optimize the error accumulation across multi-modal observation sources.

3.1 Target modeling

To model the target’s appearance and geometry, we reformulate the dynamic scene as a static object-centralized scene.

Centralization. We firstly use the pre-trained SAM [12] to separate the background and the dynamic target. Then, by establishing an object-centralized normalized coordinate [2], we decompose the complex projectile motion: the object’s autorotation is disentangled into pseudo multi-view observations, while translational displacements are eliminated.

Reconstruction. Following the 3DGS [11], we use a set of Gaussian kernels to explicitly reconstruct the appearance and geometry of the object.

Notably, geometric quality directly affects motion recovery. Therefore, the structural flaws of Gaussian representation cannot be ignored: (1) Oversize Gaussians. They frequently occur at boundaries to incorrectly fit the viewpoint variations, inducing jagged edges and spiky artifacts. (2) Discretized Gaussians. They appear distant from the target, distorting centroid computation and introducing systematic errors in motion estimation. To address these, we propose an improved point density control strategy: (1) Axial constraint: Hard pruning of Gaussians with excessive axial lengths; (2) Outlier removal: Gaussians whose distance to their nearest neighbors exceeds the average value are removed. This

can be mathematically expressed as:

$$\mathcal{G}_{\text{pruned}} = \left\{ g_i \in \mathcal{G} \left| \begin{array}{l} \max(\text{eig}(\Sigma_i)) \leq \tau_L \quad \cap \\ \min_{g_j \in \mathcal{G}} \|\mu_i - \mu_j\|_2 \leq \tau_D \cdot D_{\text{avg}} \end{array} \right. \right\} \quad (1)$$

where Σ_i and μ_i represent the covariance matrix and position of a Gaussian g_i respectively. For axial constraint, Gaussians with length of principal axis $\max(\text{eig}(\Sigma_i)) > \tau_L$ are discarded, where τ_L is a predefined threshold controlling shape anisotropy. Besides, an outlier is defined as a Gaussian whose minimum distance to other is much larger than the average distance $D_{\text{avg}} = \frac{1}{|\mathcal{G}|^2} \sum_{m,n} \|\mu_m - \mu_n\|_2$, where τ_D is a distance-based filtering factor.

During the optimization, the loss \mathcal{L}_{GS} is used to quantify the difference between the real image \hat{I} and render image I :

$$\mathcal{L}_{GS} = (1 - \lambda) \|\hat{I} - I\|_1 + \lambda \mathcal{L}_{D-SSIM} \quad (2)$$

Up to this point, we consequently obtain a Gaussian field G_0 at the centralized scale.

Registration. Finally, we register the static Gaussian G_0 at the centralized scale to the original dynamic scene, thus facilitating subsequent motion recovery. This can be achieved via a set of learnable affine transformations $T_{\text{reg}} = [\mathbf{r}, \mathbf{t}, s]$, i.e., quaternion rotation $\mathbf{r} \in \mathbb{R}^4$, translation vector $\mathbf{t} \in \mathbb{R}^3$, and constant scalar scale s . Then the aligned Gaussian field G_1 can be represented as $T_{\text{reg}} \odot G_0$. In addition to \mathcal{L}_{GS} , we further apply VGG loss \mathcal{L}_{VGG} and grid-based total variation loss \mathcal{L}_{TV} [36, 30] to achieve a better awareness for accurate registration. The total loss can be formulated as:

$$\mathcal{L}_{\text{Align}} = \lambda_1 \mathcal{L}_{GS} + \lambda_2 \mathcal{L}_{VGG} + \lambda_3 \mathcal{L}_{TV} \quad (3)$$

The optimization target is to minimize $\mathcal{L}_{\text{Align}}$ between the rendered image of G_1 and the first frame \hat{I}_0 of original dynamic scene:

$$T_{\text{reg}} = \underset{T_{\text{reg}}}{\text{argmin}} \mathcal{L}_{\text{Align}}(\mathcal{R}(T_{\text{reg}} \odot G_0), \hat{I}_0) \quad (4)$$

Finally, we obtain this set of Gaussian G_1 , which can well-represent the appearance and geometry of the object.

3.2 Physics-Enhanced Motion recovery

During the dynamic phase, we estimate 6DoF pose changes of the object in total $(n+1)$ frames, which corresponds to a sequence of temporal SE-3 transformations $T_n = [\mathbf{r}_n, \mathbf{t}_n]$. We introduce an acceleration consistency constraint to establish a direct connection between pose learning and physical priors. Additionally, we incorporate optical flow smoothing and a DSA training strategy to improve training stability.

Acceleration consistency constraint. The object moves in a constant force field, therefore its acceleration remains constant. Based on this, we first

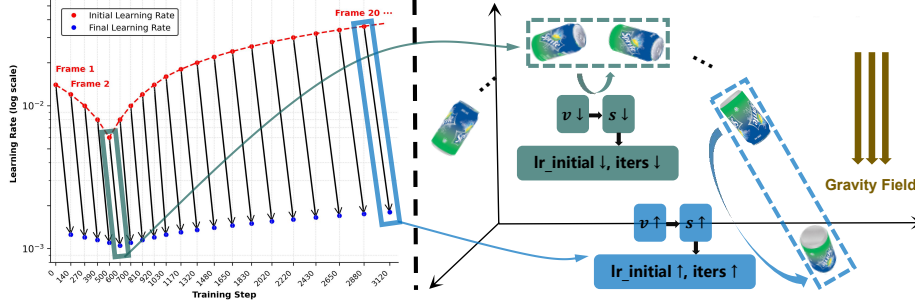


Figure 3: DSA strategy. Right: An object accelerates in a constant gravity field, with different velocity v and displacements s corresponding to each timestamp. Left: Red curve represents the initial learning rate. Blue points shows the final learning rate after exponential decay.

calculate the object's center of mass σ . Since the Gaussian have been processed isotropically, the spatial coordinates of σ can be computed as:

$$\sigma = \frac{\sum_{i=1}^N R_i^3 \mu_i}{\sum_{i=1}^N R_i^3} \quad (5)$$

where N represents the total number of Gaussian kernels, R is the radius of each kernel, and $\mu_i = [x_i, y_i, z_i]$ denotes the spatial position of the kernel. In turn, the acceleration of the object at the current moment t can be calculated as:

$$a^t = \frac{[\sigma^{(t+\Delta t)} - \sigma^t] - [\sigma^t - \sigma^{(t-\Delta t)}]}{(\Delta t)^2} \quad (6)$$

where Δt denotes the time interval between two adjacent frames. Subsequently, the acceleration \mathbf{a}^t can be decomposed into components parallel and orthogonal to the gravity direction \mathbf{g} :

$$\begin{aligned} \mathbf{a}_{\parallel}^t &= (\mathbf{a}^t \cdot \mathbf{g}) \mathbf{g}, \\ \mathbf{a}_{\perp}^t &= \mathbf{a}^t - (\mathbf{a}^t \cdot \mathbf{g}) \mathbf{g} \end{aligned} \quad (7)$$

According to the Newtonian dynamics, there should be a constant acceleration along the gravity direction, while the components orthogonal to it should remain zero:

$$\mathcal{L}_{Acc} = \|\mathbf{a}_{\parallel}^t + (a_{\perp}^{(t+\Delta t)} - a_{\perp}^t)\|_2^2 \quad (8)$$

Building upon Eq.8, we are able to effectively regularize the learning of translation components across consecutive frames, even under scale ambiguity, thereby ensuring the physical consistency of motion recovery without requiring absolute values such as gravitational acceleration.

Dynamic Simulated Annealing. As shown in Figure 3, a fixed lr_{init} struggles to adapt to varying object's velocities: excessively large lr_{init} induce training

oscillations during low-speed phases, whereas small lr_{init} hinder convergence when tracking high-speed targets. To address this velocity-displacement coupling effect, we dynamically schedule the lr_{init} according to real-time displacement.

Specifically, for a moving object with an initial velocity v_0 and constant acceleration a , the displacement during the interval from timestamp t to $(t + \Delta t)$ can be derived as:

$$\Delta s_t = (a\Delta t)t + \left[\frac{1}{2}a(\Delta t)^2 + v_0\Delta t\right] \quad (9)$$

As the initial velocity v_0 , acceleration a and the time interval Δt are constant value, thus Equation 9 establishes the linear correlation between object’s displacement Δs and timestamp t , i.e., $\Delta s \propto t$. This temporal-displacement relationship therefore requires proportional scaling of the lr_{init} with displacement. Therefore, we implement scheduling where the learned displacement from the preceding timestep governs the subsequent lr_{init} , as visualized in Figure 3.

As the iteration progresses, the Gaussians gradually approach the target spatial position. Correspondingly, the learning rate needs to be reduced so that the step gradually shrinks for finetuning. We utilized the commonly used exponential decay to achieve this. In addition, for timestamps with large displacements, we appropriately extend the number of iterations to better find the optimal solution.

In summary, we follow the DSA strategy for frame-by-frame tracking of the pose T_n during motion recovery, and the total optimization is to minimize a composite of losses:

$$T_n = \underset{T_n}{\operatorname{argmin}}(\lambda_1\mathcal{L}_{GS}(\mathcal{R}(G_n), \hat{I}_n) + \lambda_2\mathcal{L}_{Acc}) \quad (10)$$

3.3 Cross-modal Kalman fusion

Furthermore, we introduce optical flow smoothing computed based on [27] for emphasizing attention to motion variations in long-term tracking. Though some works [6] also incorporate optical flow or priors as auxiliaries, but they fail to account for the inaccurate optical flow estimation caused by degraded textures under motion blur, which in turn introduces negative effects. Differently, we design a data fusion strategy based on Kalman Filter [29] to dynamically balance the weights of observation sources, suppress cumulative error, and update the optimal estimate in real-time.

Step1-Definition: The basic elements in Kalman fusion namely the system prediction model and observations. When applied to our motion recovery process, these components correspond to the following:

- System model: Displacement prediction based on the acceleration consistency constraint (Eq.8).
- Observation 1: The displacement calculated via back-projection from the inter-frame optical flow field z_{flow}^t .

- Observation 2: The displacement of the current frame actually learned by the network z_{learn}^t .

Step2-Prediction: In the prediction step, we use the system dynamic model and previous state estimation to predict the current state, which can be formulated as:

$$\begin{aligned} \mathbf{X}_{t|t-1} &= \begin{bmatrix} \Delta s_{t|t-1} \\ v_{t|t-1} \end{bmatrix} = \mathbf{F}\mathbf{X}_{t-1|t-1} + \mathbf{B}a_k + \mathbf{w}_k, \\ \mathbf{F} &= \begin{bmatrix} 1 & \Delta t \\ 0 & 1 \end{bmatrix}, \mathbf{B} = \begin{bmatrix} \frac{1}{2}(\Delta t)^2 \\ \Delta t \end{bmatrix}, \mathbf{Q} = \begin{bmatrix} \sigma_{\Delta s}^2 & 0 \\ 0 & \sigma_v^2 \end{bmatrix} \end{aligned} \quad (11)$$

where $\mathbf{X}_{t|t-1}$ is the prediction based on the optimal estimate at previous timestamp, \mathbf{F} is the state transition matrix, \mathbf{B} is the control input matrix, and a_t is the control input calculated from Eq.6, which approximates to a_{t-1} as the system model defined. $\mathbf{Q} = \mathbb{E}[\mathbf{w}_k \mathbf{w}_k^T]$ is the covariance matrix of the process noise \mathbf{w}_k (includes noise $\sigma_{\Delta s}^2$ and σ_v^2) that describes the uncertainty of the model. The prediction covariance then can be calculated as:

$$\mathbf{P}_{t|t-1} = \mathbf{F}\mathbf{P}_{t-1|t-1}\mathbf{F}^T + \mathbf{Q} \quad (12)$$

where $\mathbf{P}_{t-1|t-1}$ is the posterior covariance of the previous state.

Step3-Correction: In the update step, we use observations (optical flow and learned displacement) to correct the predicted state. These two measurements provide direct observations of displacement, but each carries distinct noise: (1) z_{flow}^t is computed from optical flow (Eq.9), representing apparent-motion-based displacement observation. Its noise sources include texture corruption and motion blur, with noise denoted as σ_{flow}^2 . (2) z_{learn}^t derives from the optimization process (Eq. 11), based on Gaussian rendering and loss functions. Its noise originates from training oscillations, local optima, or initialization errors, with noise denoted as σ_{learn}^2 . Thus, we define the observation equation as follows:

$$\begin{aligned} \mathbf{z}_t &= \begin{bmatrix} z_{flow}^t \\ z_{learn}^t \end{bmatrix} = \mathbf{H}\mathbf{X}_{t|t} + \mathbf{v}_k, \\ \mathbf{H} &= \begin{bmatrix} 1 & 0 \\ 1 & 0 \end{bmatrix}, \mathbf{R} = \begin{bmatrix} \sigma_{flow}^2 & 0 \\ 0 & \sigma_{learn}^2 \end{bmatrix} \end{aligned} \quad (13)$$

where \mathbf{H} is the observation matrix, $\mathbf{R} = \mathbb{E}[\mathbf{v}_k \mathbf{v}_k^T]$ is the covariance of noise \mathbf{v}_k .

Step4-Update: Based on above content, we update the Kalman gain \mathbf{K}_t and the posterior covariance $\mathbf{P}_{t|t}$:

$$\mathbf{K}_t = \mathbf{P}_{t|t-1}\mathbf{H}^T(\mathbf{H}\mathbf{P}_{t|t-1}\mathbf{H}^T + \mathbf{R})^{-1} \quad (14)$$

$$\mathbf{P}_{t|t} = (\mathbf{I} - \mathbf{K}_t\mathbf{H})\mathbf{P}_{t|t-1} \quad (15)$$

Finally, we can obtain the optimal estimated value at the current timestamp:

$$\mathbf{X}_{t|t} = \mathbf{X}_{t|t-1} + \mathbf{K}_t(\mathbf{z}_t - \mathbf{H}\mathbf{X}_{t|t-1}) \quad (16)$$

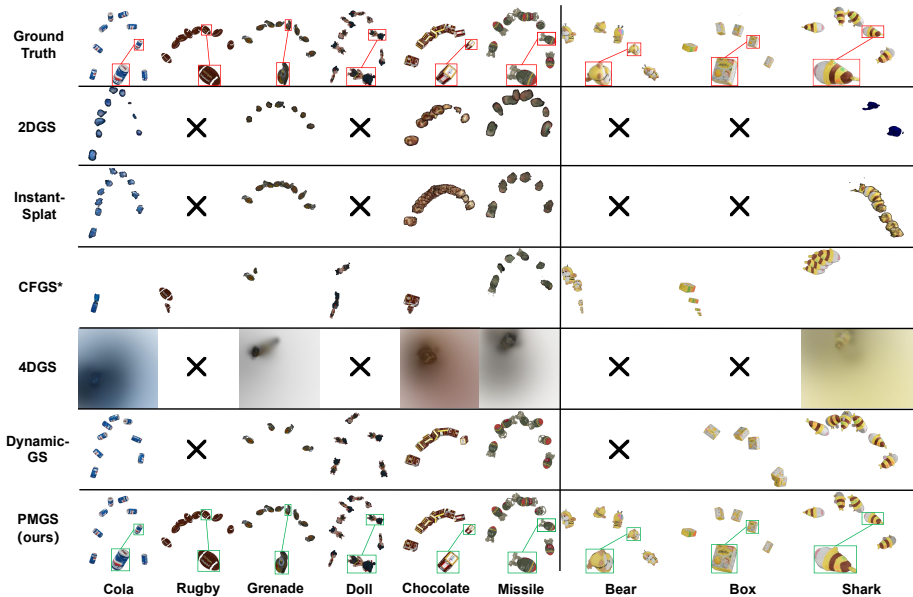


Figure 4: Qualitative comparison on both synthetic and real datasets. PMGS generalizes well across different scenarios and accurately reconstructs full-sequence motion. The displayed results are uniformly sampled, for complete and coherent motion recovery, please refer to the video on the project page.

Throughout the fusion process, we fully integrate the physical model, optical flow observations, and network outputs. The Kalman gain is used to automatically adjust the weights, thereby minimizing the error accumulation across multi-modal observation sources. Therefore, even when real-world disturbances exist or poor image quality compromises texture observations [35, 13], this strategy maintains strong robustness.

4 Experiments

4.1 Experimental Settings

Datasets. We constructed both synthetic and real-world dataset. For synthetic data, we collected 6 models from public 3D communities [1], then set up a constant gravity field in Blender. The objects were launched with a randomly set initial velocity and accompanied by autorotation. A fixed camera was used to capture the dynamic scene at 120 FPS, rendering 120 images at a resolution of 1024x1024. For the real-world dataset, we threw 3 different objects and captured the scene using a fixed camera, with an exposure time of 1/2500s, a frame rate of 60 FPS, and a resolution of 4128x2752. During training, the images were resized to below 1600 pixels. Due to the frame rate limitations of the imaging

Datasets	Source	Type	Phy.	Mono.
LaSOT [3]	Real	Rigid	×	×
D-NeRF [21]	Syn.	Def.	×	✓
HyperNeRF [20]	Real	Def.	×	✓
Neural3D [14]	Syn.	Def.	×	×
PEGASUS [17]	Syn.	Rigid	PyBullet	✓
SpringGS [36]	6S + 3R	Def.	Hooke’s Law	×
PMGS	6S + 3R	Rigid	Newton’s Law	✓

Table 1: Datasets comparison (Phy.-Whether physical prior is introduced; Mono.-Whether monocular; Syn.-Synthetic; Def.-Deformable).

	Granade			Miaale			Cda			Dall			Chocolate			Bagle			Bus			Shark			Biar			Moon		
	PSNR	SSIM	LPIPS																											
3DGS	24.82	0.895	0.153	17.42	0.714	0.205	15.97	0.847	0.195	17.99	0.792	0.218	15.19	0.758	0.275	21.56	0.830	0.185	19.72	0.973	0.172	11.57	0.794	0.161	11.78	0.823	0.201	17.34	0.825	0.202
InstantSplat	25.44	0.900	0.139	17.58	0.724	0.200	17.03	0.852	0.175	18.10	0.797	0.221	16.10	0.761	0.255	21.21	0.877	0.185	20.48	0.977	0.152	12.88	0.850	0.097	11.79	0.823	0.090	18.18	0.855	0.177
CFGS*	21.82	0.873	0.231	13.70	0.675	0.259	14.47	0.845	0.284	18.00	0.788	0.307	11.93	0.739	0.317	21.37	0.822	0.196	17.19	0.946	0.162	11.32	0.742	0.271	11.54	0.772	0.212	15.70	0.800	0.248
4DGS	20.52	0.907	0.112	22.60	0.829	0.082	20.25	0.859	0.154	23.92	0.947	0.063	17.91	0.934	0.182	Label	Label	Label	20.19	0.874	0.131	15.32	0.709	0.302	Label	Label	Label	19.11	0.866	0.156
MotionGS	23.04	0.876	0.166	19.14	0.857	0.156	15.30	0.823	0.217	22.70	0.854	0.119	16.99	0.902	0.115	17.37	0.825	0.131	15.82	0.812	0.084	10.38	0.684	0.353	11.99	0.887	0.131	17.50	0.782	0.227
DynamicGS	26.32	0.971	0.064	20.57	0.906	0.032	28.44	0.930	0.028	21.81	0.942	0.050	25.96	0.907	0.018	Label	Label	Label	18.97	0.704	0.152	24.92	0.952	0.055	Label	Label	Label	28.03	0.961	0.058
PMGS	31.58	0.967	0.011	28.87	0.915	0.025	26.50	0.940	0.014	34.38	0.959	0.014	25.01	0.924	0.020	33.72	0.954	0.012	30.45	0.974	0.019	25.07	0.952	0.094	28.64	0.959	0.059	29.35	0.949	0.029

Table 2: Comparison of video reconstruction.

device and the real-world projectile objects do not undergo sufficiently complete rotations (i.e., failing to exhibit a full 360° surface), we captured three projectile sequences for each model from the same viewpoint. Samples were then randomly selected from these sequences to perform modeling.

For reconstruction, the training/validation split strictly adheres to 3DGS. As for the motion recovery, we focus on recovering the full-sequence motion (all frames), thus no split is required. All competitors follow the aforementioned dataset division for fair metric calculation.

Furthermore, we conducted a comprehensive comparison between our proposed dataset and existing 4D datasets, as detailed in Table 1. PMGS covers both real and synthetic sources and sets the challenging monocular scenario, focusing on long-duration, large-span complex rigid motions. All motions strictly adhere to real-world physical laws, which has not been considered in many synthetic datasets.

Metrics. We evaluate video reconstruction and motion recovery separately. For **video reconstruction**, we use PSNR, SSIM, and LPIPS [28, 34]. For **motion recovery**, we compute the bounding boxes of the target object in both the real and rendered image, and then calculate the IoU, absolute trajectory error (ATE) and RMSE [33, 25, 5] to comprehensively assess the spatial accuracy of tracking and trajectory. It should be clarified that, all evaluations were computed after fully removing backgrounds.

Implementation Details. We conducted experiments in the PyTorch framework with an Nvidia RTX 4090 GPU. During the centralization phase, we cropped the target from the original data and placed it at the center of a 512x512 canvas. In the registration phase, we trained a set of $[\mathbf{r}, \mathbf{t}, s]$ to align the static Gaussian with the first frame of the dynamic scene within 10,000 iterations,

	Grenade			Missile			Cdn			Doll			Chocolate			Rugby			Box			Shark			Bee			Mean		
	IoU \uparrow	ATE \downarrow	RMSE \downarrow	IoU \uparrow	ATE \downarrow	RMSE \downarrow	IoU \uparrow	ATE \downarrow	RMSE \downarrow	IoU \uparrow	ATE \downarrow	RMSE \downarrow	IoU \uparrow	ATE \downarrow	RMSE \downarrow	IoU \uparrow	ATE \downarrow	RMSE \downarrow	IoU \uparrow	ATE \downarrow	RMSE \downarrow	IoU \uparrow	ATE \downarrow	RMSE \downarrow	IoU \uparrow	ATE \downarrow	RMSE \downarrow	IoU \uparrow	ATE \downarrow	RMSE \downarrow
CFGS*	0.249	0.550	0.692	0.203	0.129	0.218	0.154	0.533	0.563	0.310	0.358	0.459	0.318	0.574	0.610	0.094	0.562	0.604	0.079	0.202	0.425	0.252	0.425	0.458	0.199	0.319	0.364	0.206	0.426	0.478
4DGS	0.359	0.661	0.703	0.608	0.194	0.248	0.354	0.630	0.661	0.401	0.563	0.621	0.287	0.668	0.687	Failed	Failed	Failed	0.144	0.553	0.592	0.141	0.505	0.556	Failed	Failed	Failed	0.302	0.549	0.589
MotionGS	0.288	0.474	0.505	0.541	0.655	0.704	0.423	0.511	0.551	0.501	0.505	0.559	0.549	0.501	0.522	0.249	0.643	0.668	0.299	0.207	0.313	0.298	0.557	0.629	0.179	0.526	0.573	0.414	0.495	0.540
DynamicGS	0.548	0.227	0.269	0.910	0.118	0.156	0.898	0.182	0.226	0.663	0.311	0.363	0.995	0.070	0.090	Failed	Failed	Failed	0.262	0.439	0.470	0.679	0.094	0.155	Failed	Failed	Failed	0.707	0.205	0.247
PMGS	0.998	0.108	0.254	0.995	0.091	0.130	0.997	0.069	0.080	0.993	0.092	0.152	0.987	0.108	0.214	0.952	0.021	0.148	0.940	0.055	0.086	0.876	0.021	0.093	0.969	0.043	0.047	0.967	0.080	0.133

Table 3: Comparison of motion recovery.

using a learning rate of $5e-5$. This process is fast, typically taking only 2 minutes. In the motion recovery phase, the initial base learning rate applied to the frame with the minimal velocity was set to $1.0e-3$, with a base iteration count of 1000. The weights for the \mathcal{L}_{GS} , \mathcal{L}_{Acc} and \mathcal{L}_{Smooth} were set to 0.7, 0.2 and 0.1.

4.2 Comparison

We select 2DGS [8], InstantSplat [4] as **static competitors**. **Dynamic competitors** include 4DGS [30], DynamicGS [15] and MotionGS [37]. Furthermore, we employed CFGS [5] as a **baseline** by disabling its depth estimation for reconstruction, and instead inputting our pre-trained Gaussian model for purely 6DoF pose estimation comparison (symbolized as CFGS*).

Comparison of video reconstruction. We report the quantitative results in Table 2. Our algorithm demonstrates robust performance, as the proposed density control strategy effectively enhances appearance and geometric quality, thereby providing a solid foundation for dynamic reconstruction. CFGS underperforms, primarily due to inherent flaws in depth inference pipelines. For object-specific modeling under non-open scenarios, the monocular observation system yields an underdetermined solution manifold, where maintaining 3D consistency over extended spatiotemporal intervals becomes theoretically unattainable.

Comparison of motion recovery. We uniformly sample frames from complete sequences and visualize in Figure 4, and the quantitative results are reported in Table 3. PMGS performs well in all three tracking metrics, demonstrating accurate estimation of both translation and rotation. 4DGS and MotionGS exhibit obvious trajectory fractures and artifacts—typical limitations of dynamic algorithms when modeling large-scale motions. While DynamicGS demonstrates promising performance, it exhibits limited generalization capability to certain instances. For CFGS, even with our well-trained 3D model provided, the spatial position of Gaussian is incorrectly driven toward infinity under only photometric supervision to forcibly fit image similarity. These findings collectively reveal the effectiveness of physics constraints and adaptive training scheduling for recovering complex motions across large spatiotemporal domains.

Additional experimental results and extended applications are presented in Figure 5, showing the potential of PMGS in understanding and interacting with the real world.

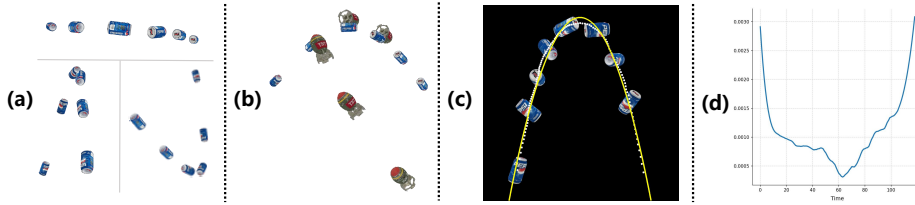


Figure 5: Extended experiments. (a) Novel views synthesis. (b) Multi-objects interaction. (c) Future motion trajectory prediction based on the 3D centroid coordinates with MLP. (d) Instantaneous displacement perception.

	Video reconstruction			Motion recovery			
	PSNR \uparrow	SSIM \uparrow	LPIPS \downarrow	IoU \uparrow	ATE \downarrow	RMSE \downarrow	Time \downarrow
CFGs*	16.82	0.799	0.249	0.206	0.426	0.478	103 mins
Model 1 (w/o density control)	24.61	0.910	0.089	0.635	0.334	0.791	51 mins
Model 2 (w/o L_{Acc} & DSA)	25.63	0.929	0.045	0.886	0.137	0.188	64 mins
Model 3 (w/o Kalman)	28.95	0.940	0.035	0.933	0.098	0.147	42 mins
PMGS (Ours)	29.35	0.949	0.029	0.967	0.080	0.133	48 mins

Table 4: Ablation study of different models.

4.3 Ablation Study

We conducted ablation experiments to verify the effectiveness of different novel modules.

Effectiveness of point density control. As evidenced in Table 4, Model 1 exhibits degradation, demonstrating that poor reconstruction directly compromises tracking accuracy. Incorrect geometry and appearance representations may cause target mislocalization—especially when floating Gaussian points distort the calculation of central points and bounding boxes, thus resulting in cumulative errors over time.

Effectiveness of physical constraints. Model 2 ablates L_{Acc} and DSA strategy, retaining only photometric supervision and fixed training paradigm. As shown in Figure 6, the spatial position of the object exhibits drift, and errors are observed obviously in rotational orientation. The removal of DSA significantly increases the optimization time cost, revealing the necessity of adaptive adjustment of the learning rate under high-speed displacement.

Effectiveness of Kalman fusion. The removal reduced computational cost overhead at the expense of a decrease in stability. In more challenging scenarios (e.g., under substantial time-varying force interference), the strategy’s role in ensuring robustness would be more pronounced.



Figure 6: Ablation results for different comparison models. PMGS in its complete form exhibits superior stability.

5 Conclusion

In this paper, we propose PMGS for reconstructing projectile motion over large spatiotemporal scales from monocular videos. Through a two-stage pipeline involving dynamic scene decomposition modeling and physically enhanced motion recovery, we effectively alleviate the issues of trajectory fragmentation and physical implausibility encountered by existing dynamic neural rendering methods when handling high-speed, non-linear rigid motion. Moreover, the proposed cross-modal Kalman fusion optimizes error accumulation from multi-source observations, further enhancing robustness against real-world disturbances. PMGS provides a novel perspective for the explicit modeling and understanding of the 3D physical world. In the future, we plan to delve into more challenging topics, such as achieving accurate 3D motion reconstruction under low-quality imaging conditions or changing force field environments.

References

- [1] Blender Foundation. Blender — a 3d modelling and rendering package. Blender Foundation, Amsterdam, 2018.
- [2] Wen-Hsuan Chu, Lei Ke, and Katerina Fragkiadaki. Dreamscene4d: Dynamic multi-object scene generation from monocular videos. *arXiv preprint arXiv:2405.02280*, 2024.
- [3] Heng Fan, Liting Lin, Fan Yang, Peng Chu, Ge Deng, Sijia Yu, Hexin

- Bai, Yong Xu, Chunyuan Liao, and Haibin Ling. Lasot: A high-quality benchmark for large-scale single object tracking. In *Proceedings of the IEEE/CVF conference on computer vision and pattern recognition*, pages 5374–5383, 2019.
- [4] Zhiwen Fan, Wenyan Cong, Kairun Wen, Kevin Wang, Jian Zhang, Xinghao Ding, Danfei Xu, Boris Ivanovic, Marco Pavone, Georgios Pavlakos, et al. Instantsplat: Unbounded sparse-view pose-free gaussian splatting in 40 seconds. *arXiv preprint arXiv:2403.20309*, 2(3):4, 2024.
- [5] Yang Fu, Sifei Liu, Amey Kulkarni, Jan Kautz, Alexei A Efros, and Xiaolong Wang. Colmap-free 3d gaussian splatting. In *Proceedings of the IEEE/CVF Conference on Computer Vision and Pattern Recognition*, pages 20796–20805, 2024.
- [6] Zhiyang Guo, Wen gang Zhou, Li Li, Min Wang, and Houqiang Li. Motion-aware 3d gaussian splatting for efficient dynamic scene reconstruction. *IEEE Transactions on Circuits and Systems for Video Technology*, 35:3119–3133, 2024.
- [7] Bing He, Yunuo Chen, Guo Lu, Li Song, and Wenjun Zhang. S4d: Streaming 4d real-world reconstruction with gaussians and 3d control points. *ArXiv*, abs/2408.13036, 2024.
- [8] Binbin Huang, Zehao Yu, Anpei Chen, Andreas Geiger, and Shenghua Gao. 2d gaussian splatting for geometrically accurate radiance fields. In *ACM SIGGRAPH 2024 conference papers*, pages 1–11, 2024.
- [9] Yiming Huang, Beilei Cui, Long Bai, Ziqi Guo, Mengya Xu, Mobarakol Islam, and Hongliang Ren. Endo-4dgs: Endoscopic monocular scene reconstruction with 4d gaussian splatting. In *International Conference on Medical Image Computing and Computer-Assisted Intervention*, pages 197–207. Springer, 2024.
- [10] Hanbyul Joo, Hao Liu, Lei Tan, Lin Gui, Bart Nabbe, Iain Matthews, Takeo Kanade, Shohei Nobuhara, and Yaser Sheikh. Panoptic studio: A massively multiview system for social motion capture. In *Proceedings of the IEEE international conference on computer vision*, pages 3334–3342, 2015.
- [11] Bernhard Kerbl, Georgios Kopanas, Thomas Leimkühler, and George Drettakis. 3d gaussian splatting for real-time radiance field rendering. *ACM Trans. Graph.*, 42(4):139–1, 2023.
- [12] Alexander Kirillov, Eric Mintun, Nikhila Ravi, Hanzi Mao, Chloe Roland, Laura Gustafson, Tete Xiao, Spencer Whitehead, Alexander C Berg, Wan-Yen Lo, et al. Segment anything. In *Proceedings of the IEEE/CVF international conference on computer vision*, pages 4015–4026, 2023.

- [13] Jungho Lee, Donghyeong Kim, Dogyoon Lee, Suhwan Cho, Minhyeok Lee, Wonjoon Lee, Taeh Kim, Dongyoon Wee, and Sangyoun Lee. Comogaussian: Continuous motion-aware gaussian splatting from motion-blurred images. *arXiv preprint arXiv:2503.05332*, 2025.
- [14] Tianye Li, Mira Slavcheva, Michael Zollhoefer, Simon Green, Christoph Lassner, Changil Kim, Tanner Schmidt, Steven Lovegrove, Michael Goesele, Richard Newcombe, et al. Neural 3d video synthesis from multi-view video. In *Proceedings of the IEEE/CVF conference on computer vision and pattern recognition*, pages 5521–5531, 2022.
- [15] Jonathon Luiten, Georgios Kopanas, Bastian Leibe, and Deva Ramanan. Dynamic 3d gaussians: Tracking by persistent dynamic view synthesis. In *2024 International Conference on 3D Vision (3DV)*, pages 800–809. IEEE, 2024.
- [16] Lars Mescheder, Michael Oechsle, Michael Niemeyer, Sebastian Nowozin, and Andreas Geiger. Occupancy networks: Learning 3d reconstruction in function space. In *Proceedings of the IEEE/CVF conference on computer vision and pattern recognition*, pages 4460–4470, 2019.
- [17] Lukas Meyer, Floris Erich, Yusuke Yoshiyasu, Marc Stamminger, Noriaki Ando, and Yukiyasu Domae. Pegasus: Physically enhanced gaussian splatting simulation system for 6dof object pose dataset generation. In *2024 IEEE/RSJ International Conference on Intelligent Robots and Systems (IROS)*, pages 10710–10715. IEEE, 2024.
- [18] Ben Mildenhall, Pratul P Srinivasan, Matthew Tancik, Jonathan T Barron, Ravi Ramamoorthi, and Ren Ng. Nerf: Representing scenes as neural radiance fields for view synthesis. *Communications of the ACM*, 65(1):99–106, 2021.
- [19] Jeong Joon Park, Peter Florence, Julian Straub, Richard Newcombe, and Steven Lovegrove. DeepSDF: Learning continuous signed distance functions for shape representation. In *Proceedings of the IEEE/CVF conference on computer vision and pattern recognition*, pages 165–174, 2019.
- [20] Keunhong Park, Utkarsh Sinha, Peter Hedman, Jonathan T Barron, Sofien Bouaziz, Dan B Goldman, Ricardo Martin-Brualla, and Steven M Seitz. Hypernerf: A higher-dimensional representation for topologically varying neural radiance fields. *arXiv preprint arXiv:2106.13228*, 2021.
- [21] Albert Pumarola, Enric Corona, Gerard Pons-Moll, and Francesc Moreno-Noguer. D-nerf: Neural radiance fields for dynamic scenes. In *Proceedings of the IEEE/CVF conference on computer vision and pattern recognition*, pages 10318–10327, 2021.
- [22] Jinsheng Quan, Chunshi Wang, and Yawei Luo. Particlegs: Particle-based dynamics modeling of 3d gaussians for prior-free motion extrapolation. *ArXiv*, abs/2505.20270, 2025.

- [23] René Ranftl, Alexey Bochkovskiy, and Vladlen Koltun. Vision transformers for dense prediction. In *Proceedings of the IEEE/CVF international conference on computer vision*, pages 12179–12188, 2021.
- [24] Jiawei Ren, Liang Pan, Jiaxiang Tang, Chi Zhang, Ang Cao, Gang Zeng, and Ziwei Liu. Dreamgaussian4d: Generative 4d gaussian splatting. *arXiv preprint arXiv:2312.17142*, 2023.
- [25] Denys Rozumnyi, Jiří Matas, Marc Pollefeys, Vittorio Ferrari, and Martin R Oswald. Tracking by 3d model estimation of unknown objects in videos. In *Proceedings of the IEEE/CVF International Conference on Computer Vision*, pages 14086–14096, 2023.
- [26] Liangchen Song, Anpei Chen, Zhong Li, Zhang Chen, Lele Chen, Junsong Yuan, Yi Xu, and Andreas Geiger. Nerfplayer: A streamable dynamic scene representation with decomposed neural radiance fields. *IEEE Transactions on Visualization and Computer Graphics*, 29(5):2732–2742, 2023.
- [27] Zachary Teed and Jia Deng. Raft: Recurrent all-pairs field transforms for optical flow. In *Computer Vision—ECCV 2020: 16th European Conference, Glasgow, UK, August 23–28, 2020, Proceedings, Part II 16*, pages 402–419. Springer, 2020.
- [28] Zhou Wang, Alan C Bovik, Hamid R Sheikh, and Eero P Simoncelli. Image quality assessment: from error visibility to structural similarity. *IEEE transactions on image processing*, 13(4):600–612, 2004.
- [29] Greg Welch, Gary Bishop, et al. An introduction to the kalman filter. 1995.
- [30] Guanjun Wu, Taoran Yi, Jiemin Fang, Lingxi Xie, Xiaopeng Zhang, Wei Wei, Wenyu Liu, Qi Tian, and Xinggang Wang. 4d gaussian splatting for real-time dynamic scene rendering. In *Proceedings of the IEEE/CVF conference on computer vision and pattern recognition*, pages 20310–20320, 2024.
- [31] Butian Xiong, Xiaoyu Ye, Tze Ho Elden Tse, Kai Han, Shuguang Cui, and Zhen Li. Sa-gs: Semantic-aware gaussian splatting for large scene reconstruction with geometry constrain. *ArXiv*, abs/2405.16923, 2024.
- [32] Ziyi Yang, Xinyu Gao, Wen Zhou, Shaohui Jiao, Yuqing Zhang, and Xiaogang Jin. Deformable 3d gaussians for high-fidelity monocular dynamic scene reconstruction. In *Proceedings of the IEEE/CVF conference on computer vision and pattern recognition*, pages 20331–20341, 2024.
- [33] Jiahui Yu, Yuning Jiang, Zhangyang Wang, Zhimin Cao, and Thomas Huang. Unitbox: An advanced object detection network. In *Proceedings of the 24th ACM international conference on Multimedia*, pages 516–520, 2016.

- [34] Richard Zhang, Phillip Isola, Alexei A Efros, Eli Shechtman, and Oliver Wang. The unreasonable effectiveness of deep features as a perceptual metric. In *Proceedings of the IEEE conference on computer vision and pattern recognition*, pages 586–595, 2018.
- [35] Xinyu Zhang, Haonan Chang, Yuhan Liu, and Abdeslam Boularias. Motion blender gaussian splatting for dynamic scene reconstruction. 2025.
- [36] Licheng Zhong, Hong-Xing Yu, Jiajun Wu, and Yunzhu Li. Reconstruction and simulation of elastic objects with spring-mass 3d gaussians. In *European Conference on Computer Vision*, pages 407–423. Springer, 2024.
- [37] Ruijie Zhu, Yanzhe Liang, Hanzhi Chang, Jiacheng Deng, Jiahao Lu, Wenfei Yang, Tianzhu Zhang, and Yongdong Zhang. Motions: Exploring explicit motion guidance for deformable 3d gaussian splatting. *ArXiv*, abs/2410.07707, 2024.
- [38] Zehao Zhu, Zhiwen Fan, Yifan Jiang, and Zhangyang Wang. Fsgs: Real-time few-shot view synthesis using gaussian splatting. In *European conference on computer vision*, pages 145–163. Springer, 2024.